JACS Au
AN OPEN ACCESS JOURNAL OF THE AMERICAN CHEMICAL SOCIETY

pubs.acs.org/jacsau
Article

Unleashing the Potential: High Responsivity at Room Temperature of Halide Perovskite-Based Short-Wave Infrared Detectors with Ultrabroad Bandwidth

Yuqin Qian,[#] Zhi-Chao Huang-Fu,[#] Hao Li,[#] Tong Zhang,[#] Xia Li, Sydney Schmidt, Haley Fisher, Jesse B. Brown, Avetik Harutyunyan, Hanning Chen,* Gugang Chen,* and Yi Rao*

Cite This: JACS Au 2024, 4, 3921−3930
Read Online

ACCESS | Metrics & More | Article Recommendations | Supporting Information

ABSTRACT: Short-wave infrared (SWIR) imaging systems offer remarkable advantages, such as enhanced resolution and contrast, compared to their optical counterparts. However, broader applications demand improvements in performance, notably the elimination of cryogenic temperature requirements and cost reduction in manufacturing processes. In this manuscript, we present a new development in SWIR photodetection, exploiting the potential of metal halide perovskite materials. Our work introduces a cost-effective and easily fabricated SWIR photodetector with an ultrabroad detection range from 900 to 2500 nm, a room-temperature responsivity of 1.57×10^2 A/W, and a specific detectivity of 4.18×10^{10} Jones at 1310 nm. We then performed comprehensive static and time-resolved optical and electrical measurements under ambient conditions, complemented by extensive density functional theory simulations, validating the formation of heterojunctions within the intrinsic *n*-type and extrinsic *p*-type perovskite structures. The potential of our perovskite-based SWIR materials extends from photodetectors to photovoltaic cells and introduces a possibility for high SWIR responsivity at room temperature and atmospheric pressure, which promotes its economic efficiency.

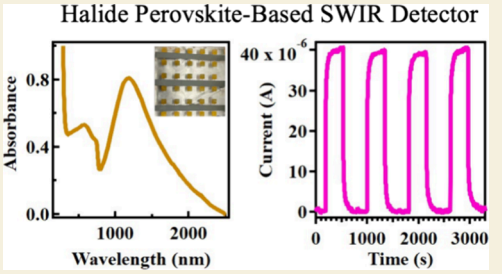

KEYWORDS: *short-wave IR detectors, short-wave IR materials, halide perovskite, heterojunctions, photoconductive detectors*

INTRODUCTION

The shortwave infrared (SWIR) spectrum, spanning wavelengths of 0.9−2.7 μm, is a critical frontier in imaging,[1] sensing,[2] security,[3] and electronics,[4] primarily due to its unique capability to produce high-resolution and high-contrast imaging. Conventional approaches to SWIR photodetection have relied heavily on narrow bandgap semiconductors and quantum structures; however, these come with their own set of limitations.[4−7] Furthermore, organic-based and quantum dot-based detectors have seen investigation, yet their SWIR responses leave much to be desired.[8−11] Certain alternative solutions, while demonstrating high SWIR responsivity, involve intricate or high-temperature fabrication processes, constraining their widespread use. Additionally, while two-dimensional graphene-based materials have shown promise, their practical application has been limited due to low light absorption, short carrier lifetimes, and the need for expensive additives.[8,9]

Organic−inorganic lead perovskite (e.g., $MAPbI_3$, MA^+: $CH_3NH_3^+$) materials, a potential game changer, have rapidly advanced into the field of optoelectronic devices,[12−18] due to their cost-effective processing,[19] exceptional defect tolerance,[15] and adjustable bandgaps.[20] To date, hybrid perovskite materials have found widespread applications in many areas, including solar cells, solar-powered water splitting systems, optically pumped lasers and light emitting diodes (LEDs), and photodetectors.[19,21−29] In particular, perovskite photodetectors in the range of visible, X-ray,[30] UV,[31] IR,[32] and terahertz,[33] have been developed with a variety of device configurations. Thin, flexible single-crystal 2D lead halide perovskites show promise for wearable electronics and photosensors.[14] However, a significant barrier to their use in the SWIR region has been the wide bandgap inherent to the perovskite materials.

In this paper, we develop a unique *p*-*n* heterojunction for SWIR detectors by interfacing intrinsic *n*-type perovskite and extrinsic *p*-type perovskites with different bandgaps by introducing hydrazinium ($NH_2NH_3^+$, HA^+) cations into the lead halide perovskite framework. The development of this material allowed us to achieve strong and tunable SWIR absorption bands. The modified perovskite was then integrated into a device which exhibits remarkable responsivity under ambient conditions and good specific detectivity throughout the SWIR region. This work provides a potential new use for perovskite materials and contributes to the discussion of

Received: July 10, 2024
Revised: September 3, 2024
Accepted: September 9, 2024
Published: September 17, 2024

https://doi.org/10.1021/jacsau.4c00621
JACS Au 2024, 4, 3921−3930

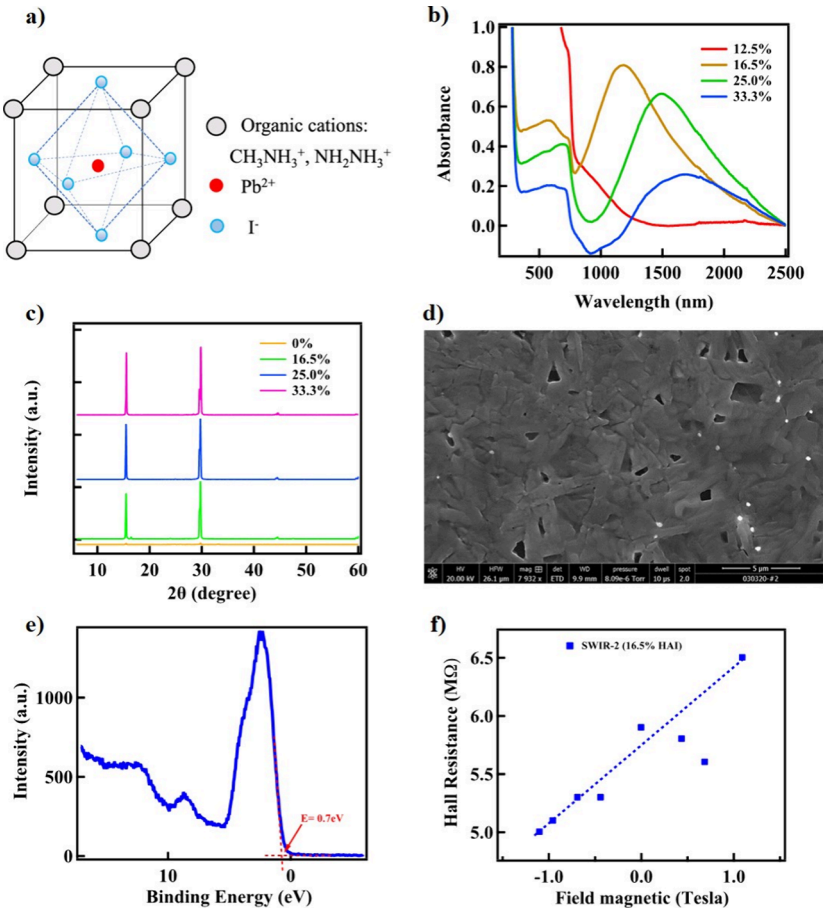

Figure 1. (a) Illustrative representations of the mixed perovskite structure $[(MAI)_{0.835}(HAI)_{0.165}]_n[PbI_2]_1$. (b) Absorption spectra of the mixed perovskite materials extending from the visible to SWIR range. (c) XRD diffractograms of the mixed perovskite featuring various HAI ratios. (d) SEM images, (e) VB-XPS spectra, and (f) Hall effect measurements of SWIR-2 incorporating 16.5% HA^+. The scale bar in panel (d) corresponds to 5 μm.

producing more efficient and cost-effective SWIR detection systems.

RESULTS

According to Goldschmidt's rule, it is possible for the hydrazinium ($NH_2NH_3^+$, HA^+) cations (effective radius ≈2.17 Å) to substitute methyl ammonium ($CH_3NH_3^+$, MA^+) cations to form mixed cations in perovskite films since HA^+ has a molecular size similar to that of MA^+.[34] HA^+ partially substitutes MA^+ in the unit cell of the 3D structure while preserving the main structure since HA^+ cations can fit the space of four adjacent corner-sharing octahedral PbI_6 to produce a close-packed 3D structure, leading to mixed cations of MA^+ and HA^+ as shown in Figure 1a. For this reason, we introduce hydrazinium cations into lead halide perovskite and engineer a *p-n* heterojunction for SWIR materials. A heterojunction is the interface between the intrinsic *n*-type perovskite and extrinsic *p*-type perovskites with different bandgaps.

Production and Examination of Perovskite-Based SWIR Materials

Initial efforts centered on the fabrication of perovskite thin films composed of mixed MA^+ and HA^+, yielding the unit cell illustrated in Figure 1a. The chemical composition of the mixed perovskite materials are formulated by $[(MA)_{1-x}(HA)_xI]_n[PbI_2]_1$. The tunable visible-SWIR absorption spectra for perovskite thin films, comprised of different proportions of HA^+ cation at a constant 2:1 mole ratio of $(MAI)_{1-x}(HAI)_x$ to PbI_2 (SWIR-2, n = 2), is displayed in Figure 1b. The percentage in this context signifies the mole ratio of $HA^+/(HA^+ + MA^+)$. First, we observed a signature semiconductor absorption peak at 780 nm, typically seen in conventional $MAPbI_3$ perovskite materials. In the SWIR region, we see that lower concentrations of HA^+ result in minimal absorption for wavelengths beyond 1000 nm. However, $HA^+ \geq 16.5\%$, a broad absorption peak appears, spanning to 2500 nm and becoming red-shifted at higher concentrations. This adjustable SWIR bands experienced a red shift as the ratio increased, and no SWIR bands were detected for ratios less than 12.5%. SWIR bands were also seen when regulating the ratio of $(MAI)_{1-x}(HAI)_x$ to PbI_2 (SWIR-3, n = 3) at 3:1 for different proportions of the HA^+ cation, as demonstrated in Figure S1a. Conversely, no significant SWIR absorption peaks were detected in the traditional *n*-type doping perovskite materials (SWIR-1, n = 1), with a stoichiometric ratio of 1:1, as shown in Figure S1b. The best outcomes in terms of both SWIR absorbance and tunability were obtained using perovskite materials with SWIR-2. Henceforth, SWIR-2 materials will be referred to as a prototype for demonstration purposes. These results indicate that the HA^+ cation may function as a dopant in the

https://doi.org/10.1021/jacsau.4c00621
JACS Au 2024, 4, 3921−3930

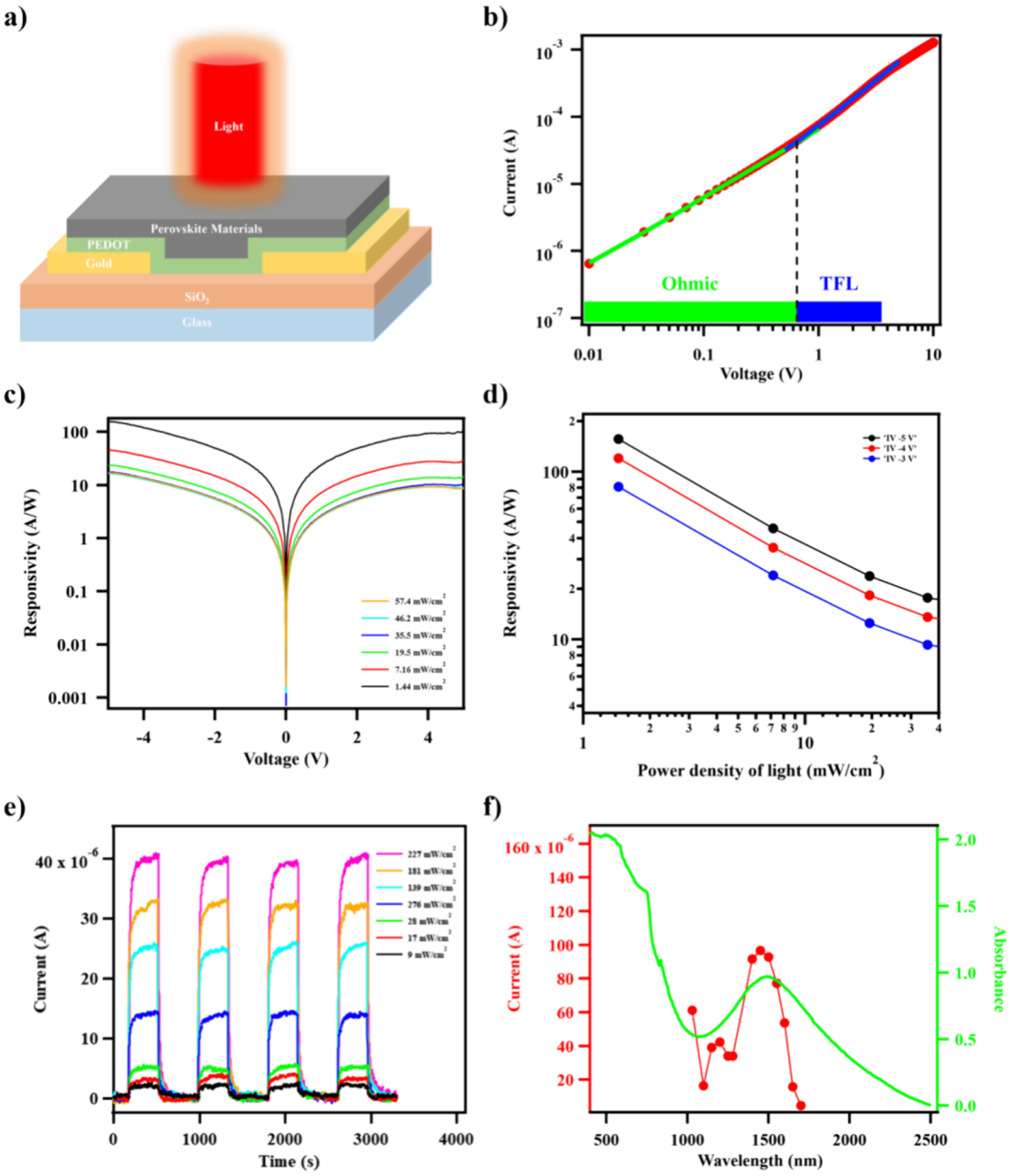

Figure 2. (a) Schematic structure for a SWIR photodetector. (b) Current−voltage curve. (c) Photoresponsivity vs voltage under different light intensities. (d) Photoresponsivity vs light intensity under different biases of −5, −4, and −3 V. (e) Photocurrent ($I_p - I_d$)−time curves with the SWIR light on and off under different light intensities at 1310 nm under a bias of −3 V. (f) Wavelength-dependent photocurrent under −3 V bias as compared to the absorption spectrum. A device of SWIR-2 (16.5% HA^+) as a representative in (b−f).

perovskite-based SWIR materials and the SWIR band predominantly arises from surplus cations of MA^+ and HA^+.

To elucidate the structure of the SWIR materials further, we characterized the perovskite thin films. X-ray diffraction (XRD) measurements were conducted to investigate the roles of excess MA^+ and HA^+ cations in the perovskite thin films. As seen in Figure 1c, two distinctive XRD peaks at 14.04° and 28.3°, corresponding to ⟨110⟩ and ⟨220⟩ indices, can be associated with the $MAPbI_3$ perovskite. It was also noted that the peak intensity escalated with an increasing mole ratio of the HA^+ cation in SWIR-2 (as seen in Figure S2). These increments in XRD intensity were ascribed to the enhanced crystallinity induced by the HA^+ doping. As depicted in Figure S2, a notable shift toward larger 2θ angles was observed in the peak of SWIR-2 with 16.5, 25.5, and 33.3% HA^+ doping as opposed to those in the SWIR-1, suggesting a contraction of the lattice with surplus HA^+ cations. Scanning electron microscopy (SEM) measurements exhibit a uniform morphology for the SWIR-2 thin films of 16.5% HA^+, as seen in Figure 1d. The band gap of perovskite-based SWIR thin films was explored using valence band X-ray photoelectron spectroscopy (VB-XPS). As shown in Figure 1e, the energy separation between the Fermi level and VB stands at 0.70 eV for SWIR-2 (16.5% HA^+). Furthermore, we executed Hall effect measurements of the SWIR materials. Figure 1f portrays a positive trend of Hall resistances with applied magnetic fields for SWIR-2 (16.5% HA^+), signifying that holes are the primary carriers in these films. The Hall effect measurements corroborate the *p*-type nature of the doped SWIR materials.

https://doi.org/10.1021/jacsau.4c00621
JACS Au 2024, 4, 3921−3930

Examining the Stability of SWIR Materials

To evaluate the long-term stability of the SWIR materials, we analyzed their surface morphology after extended storage. Figure S3 compares photographs of two glass films, SWIR-2 and regular $MAPbI_3$, exposed to ambient conditions in the dark for 100 days. Impressively, the SWIR-2 thin film exhibited remarkable stability after this period, while the pure $MAPbI_3$ showed degradation in just 18 days. The resulting crystalline SWIR perovskite materials enabled us to create high-performance SWIR photodetectors. In addition, our perovskite-based SWIR materials, which possess robust, broad-range, low-energy absorption characteristics, are perfectly suited to augment the conversion efficiency of existing perovskite-based photovoltaic cells.[35]

Fabricating Perovskite-Based SWIR Detectors

A comprehensive explanation of the device's preparation is given in the Supporting Information and is schematically depicted in Figure S4. We prepatterned Au strips as two electrical contacts, forming an active area of 30 μm wide by 1000 μm long, as seen schematically in Figure 2a. We fabricated a device with a horizontal configuration of Au/PEDOT:PSS/perovskite/Au. This unipolar photoconductive detector design allows for the extraction of photogenerated holes from the *p*-type SWIR materials. When SWIR light illuminates the detector's active area, the materials absorb photons, generating electron−hole pairs when the photon energy exceeds the bandgap. The photogenerated electrons and holes are then separated under an applied electric field and collected by opposing Au electrodes.

Evaluating the SWIR Device's Electrical Performance

The electrical performance of the SWIR device was assessed through current−voltage (I−V) measurements conducted at room temperature under ambient conditions. Figure 2b presents the I−V curve for SWIR-2 (16.5% HA^+) under dark conditions. Carrier mobility, a crucial parameter for SWIR detectors, was calculated to be 2.66×10^{-3} cm^2 V^{-1} s^{-1} using the space charge limited current (SCLC) method[36] and is detailed in the Supporting Information.

The photodetectors' photoresponsivity (R) and external quantum efficiency (EQE) were derived from photocurrents relative to applied voltages under various SWIR illumination intensities. Photoresponsivity, defined as the ratio of photocurrent to incident light power, can be mathematically expressed as follows:[29,37]

$$R = \frac{I_p - I_d}{A \times P} \tag{1}$$

where I_p represents the photocurrent under varying conditions, I_d signifies the dark current, A is the active area of the device, and P is the incident SWIR light intensity.

The EQE, which denotes the ratio of generated charge carriers to incident photons, is expressed as

$$\mathrm{EQE} = \frac{R \times hc}{e\lambda} \tag{2}$$

where h is Planck's constant, c is the speed of light, e is the electronic charge, and λ is the wavelength of the SWIR light.

Figure 2c demonstrates photoresponsivities for a typical detector made from SWIR-2 (16.5% HA^+) under different light intensities. A responsivity as high as 1.57×10^2 A/W was attained under a low light intensity of around 1.4 mW/cm^2 at 1310 nm with −5.0 V bias. This responsivity is about 3 orders of magnitude higher than that for the previously reported graphene-based photodetectors (∼0.23 A/W).[38] We also observed that the responsivities were particularly notable at a low applied bias of 1 V. Figure 2d shows photoresponsivity as a function of light intensity under various biases of −5, −4, and −3 V. The R values decrease with increased light intensity, primarily due to enhanced recombination of photogenerated carriers.

Figure 2e confirms the SWIR photoresponsivity, showing considerable differences in photocurrent responses ($I_p - I_d$) with SWIR light on and off. For instance, the SWIR device at room temperature produced photocurrents as large as 4.0×10^{-5} A under a −3.0 V bias with a power of 227 mW/cm^2 at 1310 nm. The specific detectivity, D^*, for the device was found to be around 4.18×10^{10} Jones, as calculated in the SI.[39,40] The D^* value is comparable to one of the state-of-the-art PbS quantum dot detectors.[41] Figure 2f displays the wavelength-dependent photocurrent for the SWIR-2 photodetector under ambient conditions. The measured current shows SWIR responses peaking at approximately 1450 nm, consistent with the corresponding absorption spectrum of the device. We also measured the stability of the device, measuring its relative photocurrent over time as shown in Figure S5. Here, over the first few days there was a decrease of <30% and decreased to about 20% of its maximum over 8 months. While the material does deteriorate over longer time scales under ambient conditions (vacuum-sealed at room temperature), we believe that its storage in a proper housing for the device under true vacuum would increase its stability significantly. These electrical measurements verify the ultrabroad SWIR-induced responses in the SWIR-2 devices at room temperature.

Understanding the High Responsivity Mechanism of the SWIR Device

To uncover the underlying mechanism for the high responsivity of the SWIR device, we delved into its photoconductive gain. Within a device, photoconductive gain is typically determined by the ratio of the carrier lifetime (t_{life}) and the carrier transit time within the device ($t_{transit}$). In our SWIR-2 device, with its two ohmic Au contacts, photoconductive gain measurement is accomplished under applied electric fields. From the lifetime measurements shown in Figure S6a, $t_{transit}$ was estimated to be approximately 1.3 ns. Conversely, the time of photogenerated holes extracted from Figure S6b indicates a t_{life} of around 1.6 s. This suggests that a theoretical gain, being equal to $t_{life}/t_{transit}$, could reach as high as 10^8. The corresponding EQE was calculated to be 1.4×10^2 at a 1310 nm wavelength under a bias of −5.0 V with a light power of 1.4 mW/cm^2, as illustrated in Figure S7. The majority hole carriers traversing the SWIR device maintain a short transit time, thus generating substantial photocurrent for each incident photon and a high apparent EQE. The real photoconductive gain of the devices was found to be 8.6×10^2, as described in the Supporting Information. The effective EQE is the product of the internal quantum efficiency and the photoconductive gain, which can lead to an EQE exceeding unity. The performance attributes of these devices, including SWIR responsivity, internal quantum efficiency, and specific detectivity, could be substantially elevated through strategic interface modification and meticulous optimization of material composition.[8−11,18,31,37,42−44] Furthermore, the specific detectivity could be significantly boosted by increasing the size of

https://doi.org/10.1021/jacsau.4c00621
JACS Au 2024, 4, 3921−3930

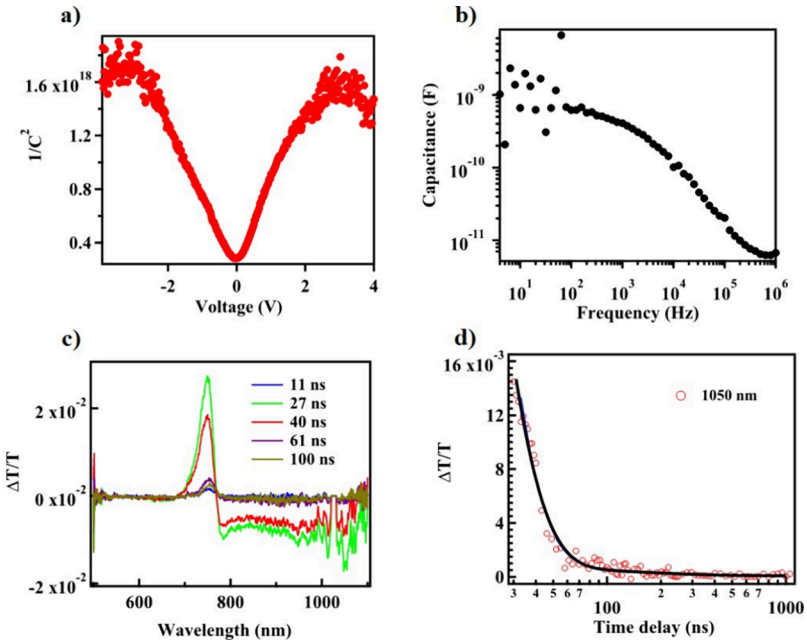

Figure 3. (a) Mott−Schottky measurements at 2 kHz. (b) Capacitance versus frequency at zero applied bias. (c) Transient absorption spectra at several time delays. (d) Kinetic trace at 1050 nm. SWIR-2 (16.5% HA^+) thin films as a representative in (a−d).

the detector, thus paving the way for future advancements in the realm of SWIR photodetection. The minority electron carriers are either trapped or in a slow transit across the SWIR device. To maintain charge neutrality inside the SWIR device, the majority hole carriers escape the device and new holes are injected from the opposite Au contact. This process can take place many times per second, resulting in large gain values. The high SWIR responsivity and gain show promising usages of the perovskite-based materials into photodetectors for practical applications. The high SWIR responsivity and EQE demonstrate the potential of these perovskite-based materials for use in photodetectors for practical applications, promising exciting developments in the field.

Exploration of the Mechanism of Perovskite-Based SWIR Materials

To understand the mechanisms underlying the outstanding performance of our SWIR detector, we carried out Mott−Schottky measurements, which are depicted in Figure 3a at a frequency of 2 kHz. The "V-shaped" characteristic in the Mott−Schottky graph was observed for the SWIR-2 device (16.5% HA^+), indicating the creation of a *p-n* junction structure within the hybrid materials. Moreover, we scrutinized whether the SWIR band stems from defects in the device via admittance measurements. Figure 3b displays capacitance ($C(\omega)$), against frequency (ω), for the SWIR-2 photodetector. Figure S8 further illustrates the density of states (DOS) as a function of energy. The DOS encompasses both an exponential distribution for the band-tail with shallow traps and a Gaussian distribution for the deeper states, indicating the existence of distinct clusters of shallow and deep traps situated at varying energy levels.[45]

Our studies utilizing transient absorption experiments have provided valuable insights into the origin of the SWIR band. As presented in Figure 3c, we examined the transient absorption spectra at different time delays for the SWIR-2 thin films. The positive transient spectral features, observed between 700 and 770 nm, are attributed to ground state bleaching (GSB), while the negative features, observed from 800 to 1000 nm, are due to excited state absorption (ESA). Notably, a distinct negative absorption band appears around 1000 to 1100 nm, indicating additional absorption following photoexcitation. This type of negative ESA differs from what is typically observed in conventional perovskite materials.[46,47] Figure 3d depicts the kinetic decay trace of photoinduced carriers at 1050 nm. Through fitting of a double exponential function, we obtained two time constants: 13.0 ± 0.8 ns and 194.3 ± 10.5 ns. The fast time constant is believed to be related to direct interband recombination in the perovskite layers, aligning with the findings from time-resolved photoluminescence displayed in Figure S6a. The slower decay lifetime likely originates from the recombination between the relaxed upper band and the lower bleached band. The presence of this longer recombination lifetime could ensure a relatively large photocurrent in the SWIR photodetectors. As a result, the combined evidence from both the transient absorption spectra and fluorescence lifetime measurements confirms the existence of additional interband recombination, as compared to traditional $MAPbI_3$. These findings not only enhance our understanding but also hint at promising applications of these materials in SWIR photodetectors.

Density Functional Theory Calculations of Perovskite-Based SWIR Materials

To further elucidate the structural origin of the SWIR band, we probed the effects of the HA^+ doping and excess cations to the perovskite crystals by using density functional theory (DFT) simulations. Band structure calculations for pristine perovskite, $CH_3NH_3PbI_3$, and mixed NH_2NH_3I-doped crystals $[(MAI)_{1-x}(HAI)_x]_2[PbI_2]_1$ were carried out. A total of five supercells, namely $A_1B_0C_1$, $A_{1.75}B_{0.25}C_1$, $A_{1.67}B_{0.33}C_1$, $A_{1.5}B_{0.5}C_1$, and $A_{1.33}B_{0.66}C_1$ (A: MAI; B: HAI; C: PbI_2) were constructed in such a way to explore a NH_2NH_3I-to-CH_3NH_3I mole ratio ranging from 0.0 to 0.5. The calculated conduction and valence band (CB and VB, respectively) edges of all materials are shown in Figure 4a and suggests the formation of

https://doi.org/10.1021/jacsau.4c00621
JACS Au 2024, 4, 3921−3930

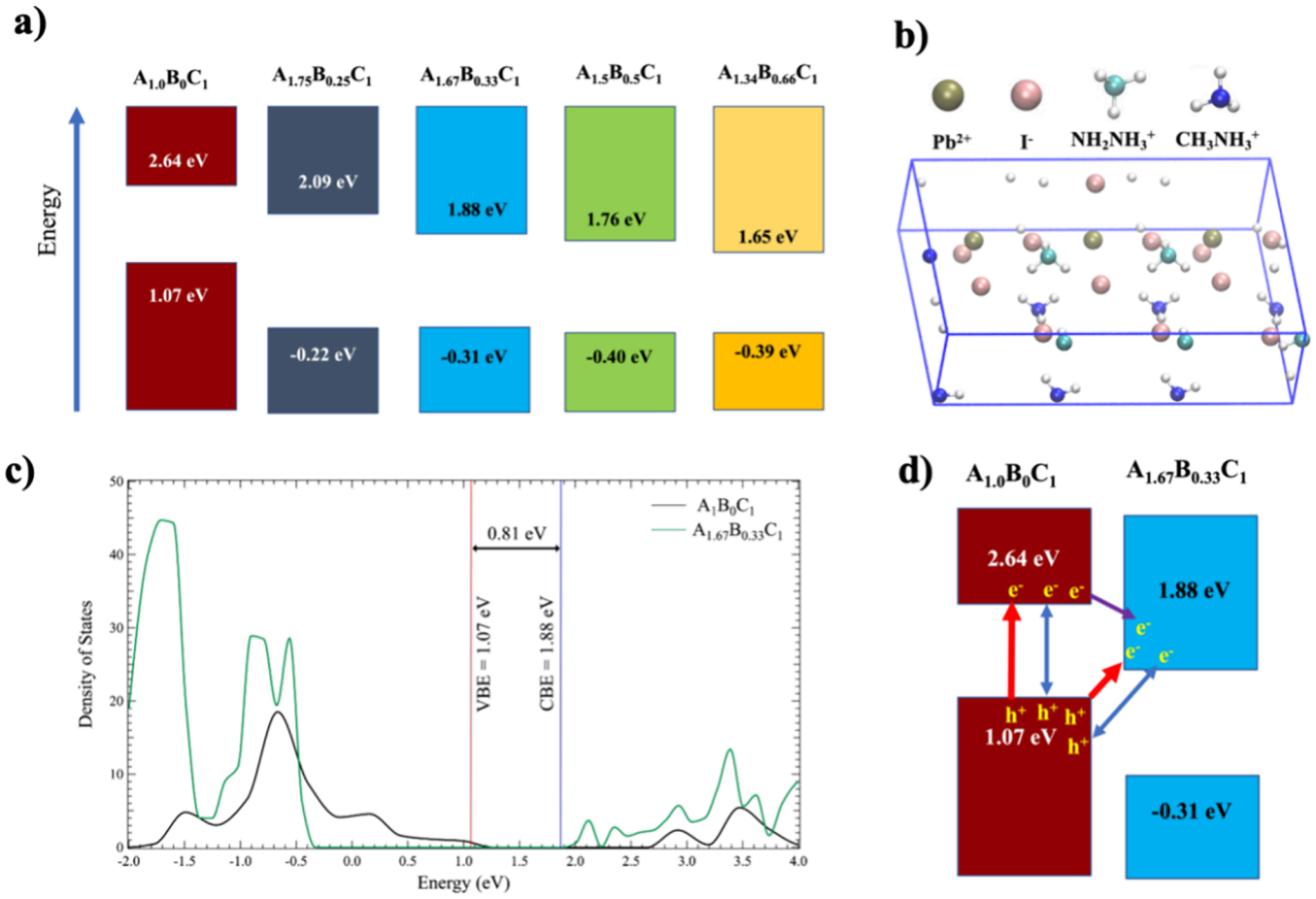

Figure 4. (a) Calculated energy level alignments for the pristine crystal $A_1B_0C_1$ and different mixed crystals $[(MAI)_{1-x}(HAI)_x]_2[PbI_2]_1$. $(A_{1-x}B_x)_2(C)_1$ represents the mixed crystals (A: MAI; B: HAI; C: PbI_2). (b) Optimized structure of $A_{1.67}B_{0.33}C_1$. (c) Density of states for $A_{1.67}B_{0.33}C_1$, as compared with that of $A_1B_0C_1$. (d) Electronic excitations and carrier recombination in a hypothetical $A_1B_0C_1/A_{1.67}B_{0.33}C_1$ mixed crystal.

heterojunctions in the mixed NH_2NH_3I-doped crystals. Figure 4b displays an example of an optimized structure of $A_{1.67}B_{0.33}C_1$. We further compared the density of states (DOS) for $A_{1.67}B_{0.33}C_1$ with that for $A_1B_0C_1$, as shown in Figure 4c. Our calculated energy gaps are well in line with our experimental results (Figure 1b). For example, when $A_1B_0C_1$ is in contact with $A_{1.67}B_{0.33}C_1$ (Figure 4d), the electronic transition from the valence band of $A_1B_0C_1$ to the conduction band of $A_{1.67}B_{0.33}C_1$ affords a much smaller energy gap of 0.81 eV. The resultant interlayer excitons have already been discovered in other type-II heterojunctions.[48] Moreover, since no electronic state is located between the conduction and valence bands of the mixed $A_1B_0C_1/A_{1.67}B_{0.33}C_1$ crystal as illustrated in its DOS profile, an intermediate band is unlikely to exist. In fact, an intermediate band is not found in any of our four other mixed supercells as shown in Figure S9, corroborating our proposed staggered-gap heterojunctions in the SWIR materials.

DISCUSSION AND CONCLUSIONS

Our current work with mixed halide perovskite materials, characterized as $[(MAI)_{1-x}(HAI)_x]_n[PbI_2]$ ($n > 1$), has led to the discovery of their robust absorption in the SWIR region and notably high carrier mobility. For the reader's convenience, Table S1 summarizes the device parameters for our photodetector as compared to other leading systems in the field. We have identified three potential mechanisms underpinning these SWIR properties: plasmonic mechanisms, intermediate band mechanisms, and heterojunction mechanisms. In general, an elevated concentration of free carriers could incite localized surface plasmon resonances, which may manifest as a plasmonic peak in the SWIR or even IR region, given a high density of delocalized free carriers. However, this effect is often induced by trapped carriers in nanocrystals or quantum dots, and our investigations reveal that the trap density in our SWIR material is not sufficiently high to facilitate the formation of surface plasmon resonance (see the Supporting Information). Therefore, plasmonic mechanisms are ruled out. We have also eliminated the possibility of an intermediate band. If an intermediate band were present, it would have an infinitely long lifetime, and no such process was observed in our measurements. Additionally, we were unable to find any evidence of an intermediate band in our computational analyses. It is then more likely that our material's properties are the result of an interperovskite HA^+-doped MA^+ *p-n* heterojunction mechanism. This conclusion is further supported by our experimental observations and computational results. As shown in Figure 4, DFT simulations showed that increasing ratios of HA^+ to MA^+ resulted in a not only decreasing VB and CV edges, but also a decreasing band gap. These changes to the electronic structure result in a redshift in the absorption spectrum and therefore and increase in

https://doi.org/10.1021/jacsau.4c00621
JACS Au 2024, 4, 3921−3930

SWIR sensitivity. The heterojunction of the $A_1B_0C_1$ and $A_{1.67}B_{0.33}C_1$ species results in broader absorption as follows: the $A_1B_0C_1$ variety has a larger bandgap and absorbs higher energy photons, resulting in the absorption band at 780 nm. The $A_{1.67}B_{0.33}C_1$ species has a moderate bandgap and absorbs moderate-energy photons. The $A_1B_0C_1/A_{1.67}B_{0.33}C_1$ heterojunction utilizes the VB of the $A_1B_0C_1$ and the CB of the $A_{1.67}B_{0.33}C_1$ and therefore absorbs lowest energy photons, allowing the absorption to push even further into the SWIR region.

These novel perovskite-based heterojunction materials demonstrate powerful and wide-ranging SWIR absorption capabilities for device applications, offering good electrical performance due to an optimal electronic match with the hole-transporting layer. In effect, this substantially reduces electron transit time, and thus promotes a significant photoconductive gain for the photodetectors. This reduction translates into a large photocurrent for every incident photon, high external quantum efficiency, elevated photoconductive gain, and superior responsivity for SWIR detectors.

The HA^+-doped perovskite materials enable high-responsivity photodetectors capable of ultrabroad SWIR absorption at room temperature. These detectors, with a responsivity as high as 1.57×10^2 A/W and a specific detectivity of 4.18×10^{10} Jones at 1310 nm, outperform traditional inorganic photodetectors and commercial photodetectors by more than 2 orders of magnitude.[49] We believe that these high-performance characteristics at room temperature in our material are afforded by the *p-n* heterojunction formed by doping the perovskite with HA^+. Moreover, our investigations into the optical properties and electrical characterization of the SWIR materials suggest the formation of a heterojunction, which our DFT simulation results corroborate.

The significance of our work lies in materials advancement for scientific and commercial uses. Our perovskite photodetectors offer high performance, affordability, and simplicity in fabrication for the SWIR wavelength range. Lastly, the devices represent an exciting prospect for a new avenue in cost-effective SWIR imaging devices that deliver high responsivity and detectivity at room temperature.

METHODS

Materials

We procured PbI_2 (99%), CH_3NH_2 (33 wt %) in ethanol, hydrazine (98%), anhydrous N, N-dimethylformamide (DMF), and isopropanol (≥99.7%) from Sigma-Aldrich. Hydroiodic acid (HI, 55−58 wt %%) was sourced from Alfa Aesar.

Synthesis of CH_3NH_3I (MAI)

We synthesized methylammonium iodide (CH_3NH_3I, MAI) by reacting hydroiodic acid with methylamine at 0 °C while stirring for 2 h. The resulting solution was evaporated under vacuum at 60 °C for 1 h. We washed the precipitate with diethyl ether three times and finally dried it at 60 °C in a vacuum oven, resulting in a white powder.

Synthesis of NH_2NH_3I (HAI)

We synthesized hydrazine ammonium iodide (NH_2NH_3I) by reacting 30 mL of hydroiodic acid with 2 mL of hydrazine at 0 °C. We slowly added the hydrazine solution, diluted with ethanol (50 v/v%), into the HI solution until a precipitate occurred. The final snow-white NH_2NH_3I powder was obtained by recrystallizing from cooled ethanol.

Preparation of SWIR Thin Films

We dissolved a mixture of MAI and HAI, and PbI_2 in DMF. While the ratio between MAI and HAI was adjusted, the total concentration of MAI and HAI was held constant at 1, 2, and 3 M compared to PbI_2 which was fixed at 0.8 M. The mixture was stirred for at least 1 h at 70 °C. We cleaned prepatterned Au glass substrates using detergent water, deionized water, acetone, ethanol, and deionized water, separately in an ultrasonic bath for 15 min each, then dried with nitrogen gas. The substrates underwent a UV-O_3 treatment for 30 min before spin-coating the hole transfer layer (HTL). We used 150 μL of PEDOT:PSS (Baytron PVP AI 4083) as the HTL material, prepared by spin-coating at 3500 rpm for 30 s and then annealed in a vacuum oven at 145 °C for 30 min. After cooling to room temperature, the substrate was transferred to a hot plate at 120 °C for 15 min. We coated the substrates with 150 μL of different cation-to-PbI_2 ratios and different HAI doping concentrations on the HTL. The spin coater was programmed to accelerate to 1000 rpm in 1 min. After, the coated substrates were annealed at 125 °C for 30 min under vacuum. The electrode contacts were exposed by removing the covered PEDOT:PSS and perovskite materials. Mott−Schottky experiments and admittance spectra were conducted with a Gamry potentiostat.

Device Preparation

We cleaned prepatterned Au glass substrates using detergent water, deionized water, acetone, ethanol, and deionized water, separately in an ultrasonic bath for 15 min each, then dried them by nitrogen gas. The substrates underwent a UV−O_3 treatment for 30 min before spin-coating the hole transfer layer (HTL). We used 150 μL of PEDOT:PSS (Baytron PVP AI 4083) as the HTL material, prepared by spin-coating at 3500 rpm for 30 s and then annealed in a vacuum oven at 145 °C for 30 min. After cooling to room temperature, the substrate was transferred to a hot plate at 120 °C for 15 min. We coated the substrates with 150 μL of different cation-to-PbI_2 ratios and different HAI doping concentrations on the HTL. The spin coater was programmed to accelerate to 1000 rpm in 1 min. After, the coated substrates were annealed at 125 °C for 30 min under vacuum. The electrode contacts were exposed by removing the covered PEDOT:PSS and perovskite materials. Mott−Schottky experiments and admittance spectra were conducted with a potentiostat (Gamry).

Material Characterization

We measured XRD with a Bruker D8 Discover X-ray diffractometer. A typical spectrum was scanned from 10° to 40° with a step size of 0.05° and a scan speed of 1.0° per second. We collected the UV and SWIR absorbance spectra using a spectrophotometer (Varia Cary 5000 UV−vis-NIR spectrometer) in the range of 300 nm-2500 nm. A field emission SEM (FEI Quanta 450 FEG) was used to investigate the surface morphology of the films. We performed nanosecond transient absorption spectroscopy characterizations using a home-built setup with a 100 kHz fiber amplifier (Light Conversion). We used an externally triggered laser of 450 nm (Thorlabs) as a pump. A digital delay generator (DG-535) served as a time delay between the pump and the probe. Time-resolved fluorescence lifetime measurements were obtained under excitation by 515 nm pulsed laser (Light Conversion) and detected by a time-correlated single photon counter (PicoQuant Gmbh). We measured current density−voltage curves for SCLC analysis using a Keithley 2401 source meter, with a scanning speed of 0.1 V s^{-1}.

Detector Performance Measurements

For SWIR photodetector performance, we used a 1310 nm laser as the source with a tunable output by a neutral density filter and spot size of 0.95 cm^2. A Keithley 2401 source meter was used to apply bias voltages and record currents. We used a light source (LPSC-1310-FC, Thorlabs, USA) to produce the 1310 nm laser. In addition, we carried out wavelength-dependent experiments with a pulsed 100 kHz laser. The tunable SWIR pulse were generated from an optical parametric amplifier (Light Conversion). We conducted all SWIR response characterization directly under ambient conditions in the dark to minimize interference from ambient light. We kept the device under dark conditions and placed it in a shielding box to decrease

https://doi.org/10.1021/jacsau.4c00621
JACS Au 2024, 4, 3921−3930

environmental disturbance. We extracted the noise current from the dark current recorded by a source meter (Keithley 2401) and applied a Fourier transform. We recorded the photoresponse of the SWIR photodetector using a Keithley 2401 source meter under different bias voltages. We measured the light intensity by a Newport 1916-R Optical Power Meter.

Theoretical Calculations

We selected the α-phase (black phase) perovskite with remarkable photovoltaic properties as our pure semiconductor for doping, while we chose the metal-free NH_2NH_3I group as our dopants to narrow the perovskite's band gap through controllable doping. The crystal structure of α-phase perovskite features a 6.31 Å × 6.31 Å × 6.31 Å cubic unit cell as determined by time-of-flight neutron and synchrotron X-ray power diffraction at room temperature. Given the chemical composition of α-phase perovskite is $CH_3NH_3IPbI_2$, we constructed its NH_2NH_3I-doped supercell by replacing some CH_3NH_3I moieties with NH_2NH_3I groups to afford a formula as $(A_{1-x}B_x)_2C$ where A = CH_3NH_3I, B= NH_2NH_3I, and C= PbI_2. As an example, we removed two PbI_2 moieties from a unit cell of a 2 × 2 × 1 super cell of α-phase perovskite, followed by substituting a CH_3NH_3I group with a NH_2NH_3I moiety to form an $A_{1.5}B_{0.5}C_1$ crystal. We constructed a total of five $(A_{1-x}B_x)_2C_1$ supercells, namely $A_2B_0C_1$, $A_{1.75}B_{0.25}C_1$, $A_{1.67}B_{0.33}C_1$, $A_{1.5}B_{0.5}C_1$, and $A_{1.33}B_{0.66}C_1$ in such a way to explore a NH_2NH_3I-to-CH_3NH_3I mole ratio ranging from 0.0 to 0.5. For each doped supercell, we first ascertained its initial atomic positions by the cluster expansion formalism using the Alloy Theoretic Automated Toolkit (ATAT) before determining its optimized cell size and atomic positions by the VASP software with HSE06 exchange-correlation functional, projector augmented-wave pseudopotential, spin−orbit coupling, plane-wave basis set, and 4 × 4 × 4 Monkhorst−Pack k-point sampling mesh. We evaluated each supercell's band structure alongside its density of states (DOS) (Figure S9). As shown by the DOS for the pristine α-phase perovskite (Figure 4a), our calculated band gap of 1.57 eV aligns well with the experimental value of 1.55 eV. It is noted that although our calculated density of states was smoothed by a Lorentzian function with a full-width-at-half-maximum of 0.1 eV, the VBE and CBE were ascertained from the presmoothed data for the highest occupied and the lowest virtual electronic orbitals.

■ ASSOCIATED CONTENT

Supporting Information

The Supporting Information is available free of charge at https://pubs.acs.org/doi/10.1021/jacsau.4c00621.

> Assessment of trap density and mobility, derivation of photoconductive gain and external quantum efficiency, specific detectivity, density of states computations, additional experimental data including absorption from different organic:inorganic ratios, X-ray diffraction patterns from detector materials, photographs of the detector during stability tests, spin-coating procedures, fluorescence lifetime data, fluence-dependent external quantum efficiency data, density of states as a function of energy, density of states computations for different hydrazine doping, and comparison of device properties to relevant literature (PDF)

■ AUTHOR INFORMATION

Corresponding Authors

Hanning Chen − *Texas Advanced Computing Center, the University of Texas at Austin, Austin, Texas 78758, United States;* orcid.org/0000-0003-3568-8039; Email: hchen@tacc.utexas.edu

Gugang Chen − *Honda Research Institute, USA, Inc., San Jose, California 95134, United States;* orcid.org/0000-0003-3798-320X; Email: gchen@honda-ri.com

Yi Rao − *Department of Chemistry and Biochemistry, Utah State University, Logan, Utah 84322, United States;* orcid.org/0000-0001-9882-1314; Email: yi.rao@usu.edu

Authors

Yuqin Qian − *Department of Chemistry and Biochemistry, Utah State University, Logan, Utah 84322, United States*

Zhi-Chao Huang-Fu − *Department of Chemistry and Biochemistry, Utah State University, Logan, Utah 84322, United States*

Hao Li − *Department of Chemistry and Biochemistry, Utah State University, Logan, Utah 84322, United States*

Tong Zhang − *Department of Chemistry and Biochemistry, Utah State University, Logan, Utah 84322, United States*

Xia Li − *Department of Chemistry and Biochemistry, Utah State University, Logan, Utah 84322, United States*

Sydney Schmidt − *Department of Chemistry and Biochemistry, Utah State University, Logan, Utah 84322, United States*

Haley Fisher − *Department of Chemistry and Biochemistry, Utah State University, Logan, Utah 84322, United States*

Jesse B. Brown − *Department of Chemistry and Biochemistry, Utah State University, Logan, Utah 84322, United States*

Avetik Harutyunyan − *Honda Research Institute, USA, Inc., San Jose, California 95134, United States*

Complete contact information is available at: https://pubs.acs.org/10.1021/jacsau.4c00621

Author Contributions

#Y.Q.Q., Z.C.H.F., H.L., and T.Z. contributed equally to this work. Y.R., G.C., and A.H. conceived and supervised the project. H.L. and X.L. conducted early experiments on material preparation and device fabrication. Y.Q., Z.C.H.F., and T.Z. performed material preparation, device fabrication, characterizations, and device optimization after H.L. and X.L. left. Y.R., H.L., Y.Q.Q., X.L., Z.C.H.F., and T.Z. analyzed the data. Y.Q., Z.C.H.F., and T.Z. also conducted transient absorption, electrochemical measurements, and time-resolved photoluminescence characterizations. H.N.C. conducted computational calculations. Y.Q.Q., S.S., H.L., and J.B. drafted the manuscript. Y.R., G.C., H.N.C., and A.H. revised the paper. All authors provided comments on the manuscript.

Notes

The authors declare no competing financial interest.

■ ACKNOWLEDGMENTS

We acknowledge the supports from Honda Research Institute USA, Inc. and the National Science Foundation under Grant No. [2045084]. Computational resources were provided by the Argonne Leadership Computing Facilities at Argonne National Laboratory under Department of Energy contract DE-AC-06CH11357 and by the Extreme Science and Engineering Discovery Environment at Texas Advanced Computing Center under National Science Foundation contract TG-CHE130008. Gold sputtering was performed by Dr. T.-C. Shen at the Nanoscale Device Laboratory at USU.

REFERENCES

(1) Naczynski, D. J.; Tan, M. C.; Zevon, M.; Wall, B.; Kohl, J.; Kulesa, A.; Chen, S.; Roth, C. M.; Riman, R. E.; Moghe, P. V. Rare-earth-doped biological composites as in vivo shortwave infrared reporters. *Nat. Commun.* **2013**, *4*, 2199.

(2) Chen, D.; Huang, J.; Jackson, T. J. Vegetation water content estimation for corn and soybeans using spectral indices derived from MODIS near- and short-wave infrared bands. *Remote Sensing of Environment* **2005**, *98* (2−3), 225−236.

(3) Krapels, K.; Driggers, R. G.; Larson, P.; Garcia, J.; Walden, B.; Agheera, S.; Deaver, D.; Hixson, J.; Boettcher, E. Small craft ID criteria (N50/V50) for short wave infrared sensors in maritime security. In *Infrared Imaging Systems: Design, Analysis, Modeling, and Testing XIX*; SPIE: 2008 Vol. *6941*, pp 47−57.

(4) Stange, D.; von den Driesch, N.; Rainko, D.; Roesgaard, S.; Povstugar, I.; Hartmann, J.-M.; Stoica, T.; Ikonic, Z.; Mantl, S.; Grützmacher, D.; Buca, D. Short-wave infrared LEDs from GeSn/SiGeSn multiple quantum wells. *Optica* **2017**, *4* (2), 185.

(5) Zhang, D.; Xue, C.; Cheng, B.; Su, S.; Liu, Z.; Zhang, X.; Zhang, G.; Li, C.; Wang, Q. High-responsivity GeSn short-wave infrared p-i-n photodetectors. *Appl. Phys. Lett.* **2013**, *102* (14), 141111.

(6) Ting, D.; Soibel, A.; Keo, S.; Rafol, S.; Mumolo, J.; Liu, J.; Hill, C.; Khoshakhlagh, A.; Hoglund, L.; Luong, E.; Gunapala, S. Development of quantum well, quantum dot, and type II superlattice infrared photodetectors. *Journal of Applied Remote Sensing* **2014**, *8* (1), No. 084998.

(7) Nair, R. R.; Blake, P.; Grigorenko, A. N.; Novoselov, K. S.; Booth, T. J.; Stauber, T.; Peres, N. M. R.; Geim, A. K. Fine Structure Constant Defines Visual Transparency of Graphene. *Science* **2008**, *320* (5881), 1308−1308.

(8) Wu, Z.; Li, N.; Eedugurala, N.; Azoulay, J. D.; Leem, D.-S.; Ng, T. N. Noise and detectivity limits in organic shortwave infrared photodiodes with low disorder. *npj Flexible Electronics* **2020**, *4* (1), 6.

(9) Li, Q.; Guo, Y.; Liu, Y. Exploration of Near-Infrared Organic Photodetectors. *Chem. Mater.* **2019**, *31* (17), 6359−6379.

(10) Hu, W.; Cong, H.; Huang, W.; Huang, Y.; Chen, L.; Pan, A.; Xue, C. Germanium/perovskite heterostructure for high-performance and broadband photodetector from visible to infrared telecommunication band. *Light Sci. Appl.* **2019**, *8*, 106.

(11) Sreeshma, D.; Janani, B.; Jagtap, A.; Abhale, A.; Rao, K. S. R. K. Defect studies on short-wave infrared photovoltaic devices based on HgTe nanocrystals/TiO2 heterojunction. *Nanotechnology* **2020**, *31* (38), 385701.

(12) Moon, D. E.; Tazik, S. K.; Wierszewski, J. G.; Gomer, N. R.; Nelson, M. P. Novel use of shortwave infrared hyperspectral imaging for standoff detection of explosives and narcotics in room clearing applications. In *Next-Generation Spectroscopic Technologies XI*; SPIE: 2018 Vol. *10657*, pp 161−167. .

(13) Burschka, J.; Pellet, N.; Moon, S. J.; Humphry-Baker, R.; Gao, P.; Nazeeruddin, M. K.; Gratzel, M. Sequential deposition as a route to high-performance perovskite-sensitized solar cells. *Nature* **2013**, *499* (7458), 316−319.

(14) Jeon, N. J.; Noh, J. H.; Kim, Y. C.; Yang, W. S.; Ryu, S.; Seok, S. I. Solvent engineering for high-performance inorganic-organic hybrid perovskite solar cells. *Nat. Mater.* **2014**, *13* (9), 897−903.

(15) Im, J. H.; Jang, I. H.; Pellet, N.; Gratzel, M.; Park, N. G. Growth of CH3NH3PbI3 cuboids with controlled size for high-efficiency perovskite solar cells. *Nat. Nanotechnol* **2014**, *9* (11), 927−932.

(16) Chen, H. W.; Sakai, N.; Jena, A. K.; Sanehira, Y.; Ikegami, M.; Ho, K. C.; Miyasaka, T. A Switchable High-Sensitivity Photodetecting and Photovoltaic Device with Perovskite Absorber. *J. Phys. Chem. Lett.* **2015**, *6* (9), 1773−1779.

(17) Li, F.; Ma, C.; Wang, H.; Hu, W.; Yu, W.; Sheikh, A. D.; Wu, T. Ambipolar solution-processed hybrid perovskite phototransistors. *Nat. Commun.* **2015**, *6*, 8238.

(18) Xie, C.; You, P.; Liu, Z.; Li, L.; Yan, F. Ultrasensitive broadband phototransistors based on perovskite/organic-semiconductor vertical heterojunctions. *Light: Science & Applications* **2017**, *6* (8), e17023−e17023.

(19) Tan, Z. K.; Moghaddam, R. S.; Lai, M. L.; Docampo, P.; Higler, R.; Deschler, F.; Price, M.; Sadhanala, A.; Pazos, L. M.; Credgington, D.; Hanusch, F.; Bein, T.; Snaith, H. J.; Friend, R. H. Bright light-emitting diodes based on organometal halide perovskite. *Nat. Nanotechnol* **2014**, *9* (9), 687−692.

(20) Kang, J.; Wang, L. W. High Defect Tolerance in Lead Halide Perovskite CsPbBr3. *J. Phys. Chem. Lett.* **2017**, *8* (2), 489−493.

(21) Vassilakopoulou, A.; Papadatos, D.; Zakouras, I.; Koutselas, I. Mixtures of quasi-two and three dimensional hybrid organic-inorganic semiconducting perovskites for single layer LED. *J. Alloys Compd.* **2017**, *692*, 589−598.

(22) Yu, J. C.; Kim, D. B.; Jung, E. D.; Lee, B. R.; Song, M. H. High-performance perovskite light-emitting diodes via morphological control of perovskite films. *Nanoscale* **2016**, *8* (13), 7036−7042.

(23) Meng, L.; Yao, E. P.; Hong, Z.; Chen, H.; Sun, P.; Yang, Z.; Li, G.; Yang, Y. Pure Formamidinium-Based Perovskite Light-Emitting Diodes with High Efficiency and Low Driving Voltage. *Adv. Mater.* **2017**, *29* (4), 1603826.

(24) Wang, J.; Wang, N.; Jin, Y.; Si, J.; Tan, Z. K.; Du, H.; Cheng, L.; Dai, X.; Bai, S.; He, H.; Ye, Z.; Lai, M. L.; Friend, R. H.; Huang, W. Interfacial control toward efficient and low-voltage perovskite light-emitting diodes. *Adv. Mater.* **2015**, *27* (14), 2311−2316.

(25) Hoye, R. L.; Chua, M. R.; Musselman, K. P.; Li, G.; Lai, M. L.; Tan, Z. K.; Greenham, N. C.; MacManus-Driscoll, J. L.; Friend, R. H.; Credgington, D. Enhanced performance in fluorene-free organometal halide perovskite light-emitting diodes using tunable, low electron affinity oxide electron injectors. *Adv. Mater.* **2015**, *27* (8), 1414−1419.

(26) Shen, L.; Fang, Y.; Wang, D.; Bai, Y.; Deng, Y.; Wang, M.; Lu, Y.; Huang, J. A Self-Powered, Sub-nanosecond-Response Solution-Processed Hybrid Perovskite Photodetector for Time-Resolved Photoluminescence-Lifetime Detection. *Adv. Mater.* **2016**, *28* (48), 10794−10800.

(27) Gong, M.; Liu, Q.; Cook, B.; Kattel, B.; Wang, T.; Chan, W.-L.; Ewing, D.; Casper, M.; Stramel, A.; Wu, J. Z. All-Printable ZnO Quantum Dots/Graphene van der Waals Heterostructures for Ultrasensitive Detection of Ultraviolet Light. *ACS Nano* **2017**, *11* (4), 4114−4123.

(28) Rao, H. S.; Li, W. G.; Chen, B. X.; Kuang, D. B.; Su, C. Y. In Situ Growth of 120 cm(2) CH(3) NH(3) PbBr(3) Perovskite Crystal Film on FTO Glass for Narrowband-Photodetectors. *Adv. Mater.* **2017**, *29* (16), 1602639.

(29) García de Arquer, F. P.; Armin, A.; Meredith, P.; Sargent, E. H. Solution-processed semiconductors for next-generation photodetectors. *Nature Reviews Materials* **2017**, *2* (3), 16100.

(30) Pan, W.; Wu, H.; Luo, J.; Deng, Z.; Ge, C.; Chen, C.; Jiang, X.; Yin, W.-J.; Niu, G.; Zhu, L.; Yin, L.; Zhou, Y.; Xie, Q.; Ke, X.; Sui, M.; Tang, J. Cs2AgBiBr6 single-crystal X-ray detectors with a low detection limit. *Nat. Photonics* **2017**, *11* (11), 726−732.

(31) Adinolfi, V.; Ouellette, O.; Saidaminov, M. I.; Walters, G.; Abdelhady, A. L.; Bakr, O. M.; Sargent, E. H. Fast and Sensitive Solution-Processed Visible-Blind Perovskite UV Photodetectors. *Adv. Mater.* **2016**, *28* (33), 7264−7268.

(32) Xu, X.; Chueh, C. C.; Jing, P.; Yang, Z.; Shi, X.; Zhao, T.; Lin, L. Y.; Jen, A. K. Y. High-Performance Near-IR Photodetector Using Low-Bandgap $MA_{0.5}FA_{0.5}Pb_{0.5}Sn_{0.5}I_3$ Perovskite. *Adv. Funct. Mater.* **2017**, *27* (28), 1701053.

(33) Rogalski, A.; Kopytko, M.; Martyniuk, P. Two-dimensional infrared and terahertz detectors: Outlook and status. *Applied Physics Reviews* **2019**, *6* (2), No. 021316.

(34) You, J.; Wang, M.; Xu, C.; Yao, Y.; Zhao, X.; Liu, D.; Dong, J.; Guo, P.; Xu, G.; Luo, C.; Zhong, Y.; Song, Q. Hydrazine dihydrochloride as a new additive to promote the performance of tin-based mixed organic cation perovskite solar cells. *Sustainable Energy & Fuels* **2021**, *5* (10), 2660−2667.

(35) Tan, Q.; Li, Z.; Luo, G.; Zhang, X.; Che, B.; Chen, G.; Gao, H.; He, D.; Ma, G.; Wang, J.; Xiu, J.; Yi, H.; Chen, T.; He, Z. Inverted

https://doi.org/10.1021/jacsau.4c00621
JACS Au 2024, 4, 3921−3930

perovskite solar cells using dimethylacridine-based dopants. *Nature* **2023**, *620* (7974), 545−551.
(36) Duijnstee, E. A.; Ball, J. M.; Le Corre, V. M.; Koster, L. J. A.; Snaith, H. J.; Lim, J. Toward Understanding Space-Charge Limited Current Measurements on Metal Halide Perovskites. *ACS Energy Letters* **2020**, *5* (2), 376−384.
(37) Guan, X.; Yu, X.; Periyanagounder, D.; Benzigar, M. R.; Huang, J.-K.; Lin, C.-H.; Kim, J.; Singh, S.; Hu, L.; Liu, G.; Li, D.; He, J.-H.; Yan, F.; Wang, Q. J.; Wu, T. Recent Progress in Short- to Long-Wave Infrared Photodetection Using 2D Materials and Heterostructures. *Advanced Optical Materials* **2021**, *9* (4), 2001708.
(38) Chen, Z.; Cheng, Z.; Wang, J.; Wan, X.; Shu, C.; Tsang, H. K.; Ho, H. P.; Xu, J.-B. High Responsivity, Broadband, and Fast Graphene/Silicon Photodetector in Photoconductor Mode. *Advanced Optical Materials* **2015**, *3* (9), 1207−1214.
(39) Fu, J.; Nie, C.; Sun, F.; Li, G.; Wei, X. Photodetectors Based on Graphene−Semiconductor Hybrid Structures: Recent Progress and Future Outlook. *Advanced Devices & Instrumentation* **2023**, *4*, No. 0031.
(40) Fu, J.; Nie, C.; Sun, F.; Li, G.; Shi, H.; Wei, X. Bionic visual-audio photodetectors with in-sensor perception and preprocessing. *Science Advances* **2024**, *10* (7), No. eadk8199.
(41) Zhang, Y.; Vafaie, M.; Xu, J.; Pina, J. M.; Xia, P.; Najarian, A. M.; Atan, O.; Imran, M.; Xie, K.; Hoogland, S.; Sargent, E. H. Electron-Transport Layers Employing Strongly Bound Ligands Enhance Stability in Colloidal Quantum Dot Infrared Photodetectors. *Adv. Mater.* **2022**, *34* (47), 2206884.
(42) Liu, C.-H.; Chang, Y.-C.; Norris, T. B.; Zhong, Z. Graphene photodetectors with ultra-broadband and high responsivity at room temperature. *Nat. Nanotechnol.* **2014**, *9* (4), 273−278.
(43) Dong, R.; Fang, Y.; Chae, J.; Dai, J.; Xiao, Z.; Dong, Q.; Yuan, Y.; Centrone, A.; Zeng, X. C.; Huang, J. High-Gain and Low-Driving-Voltage Photodetectors Based on Organolead Triiodide Perovskites. *Adv. Mater.* **2015**, *27* (11), 1912−1918.
(44) Rogalski, A.; Kopytko, M.; Martyniuk, P. Two-dimensional infrared and terahertz detectors: Outlook and status. *Appl. Phys. Rev.* **2019**, *6* (2), No. 021316.
(45) Boix, P. P.; Garcia-Belmonte, G.; Muñecas, U.; Neophytou, M.; Waldauf, C.; Pacios, R. Determination of gap defect states in organic bulk heterojunction solar cells from capacitance measurements. *Appl. Phys. Lett.* **2009**, *95* (23), 233302.
(46) Guo, Z.; Wan, Y.; Yang, M.; Snaider, J.; Zhu, K.; Huang, L. Long-range hot-carrier transport in hybrid perovskites visualized by ultrafast microscopy. *Science* **2017**, *356* (6333), 59−62.
(47) Yang, Y.; Ostrowski, D. P.; France, R. M.; Zhu, K.; van de Lagemaat, J.; Luther, J. M.; Beard, M. C. Observation of a hot-phonon bottleneck in lead-iodide perovskites. *Nat. Photonics* **2016**, *10* (1), 53−59.
(48) Jiang, Y.; Chen, S.; Zheng, W.; Zheng, B.; Pan, A. Interlayer exciton formation, relaxation, and transport in TMD van der Waals heterostructures. *Light: Science & Applications* **2021**, *10* (1), 72.
(49) Wang, Y.; Peng, L.; Schreier, J.; Bi, Y.; Black, A.; Malla, A.; Goossens, S.; Konstantatos, G. Silver telluride colloidal quantum dot infrared photodetectors and image sensors. *Nat. Photonics* **2024**, *18* (3), 236−242.

https://doi.org/10.1021/jacsau.4c00621
JACS Au 2024, 4, 3921−3930